

Faraday rotation measures of northern-hemisphere pulsars using CHIME/Pulsar

C. Ng¹, A. Pandhi², A. Naidu^{3,4}, E. Fonseca^{3,4}, V. M. Kaspi^{3,4}, K. W. Masui^{5,6},
R. Mckinven^{1,2}, A. Renard¹, P. Scholz^{1,7}, I. H. Stairs⁸, S. P. Tendulkar^{3,4}, K. Vanderlinde¹,

¹*Dunlap Institute for Astronomy and Astrophysics, University of Toronto, 50 St. George Street, Toronto, ON M5S 3H4, Canada*

²*David A. Dunlap Institute Department of Astronomy & Astrophysics, University of Toronto, 50 St. George Street, Toronto, ON M5S 3H4, Canada*

³*Department of Physics, McGill University, 3600 rue University, Montréal, QC H3A 2T8, Canada*

⁴*McGill Space Institute, McGill University, 3550 rue University, Montréal, QC H3A 2A7, Canada*

⁵*MIT Kavli Institute for Astrophysics and Space Research, Massachusetts Institute of Technology, 77 Massachusetts Ave, Cambridge, MA 02139, USA*

⁶*Department of Physics, Massachusetts Institute of Technology, Cambridge, 77 Massachusetts Ave, Massachusetts 02139, USA*

⁷*Dominion Radio Astrophysical Observatory, Herzberg Astronomy & Astrophysics Research Centre, National Research Council Canada, P.O. Box 11717, Stn. Science, Ottawa, ON K1A 0R6, Canada*

⁸*Dept. of Physics and Astronomy, University of British Columbia, 6224 Agricultural Road, Vancouver, BC V6T 1Z1, Canada*

Accepted XXX. Received YYY; in original form ZZZ

ABSTRACT

Using commissioning data from the first year of operation of the Canadian Hydrogen Intensity Mapping Experiment’s (CHIME) Pulsar backend system, we conduct a systematic analysis of the Faraday Rotation Measure (RM) of the northern hemisphere pulsars detected by CHIME. We present 55 new RMs as well as obtain improved RM uncertainties for 25 further pulsars. CHIME’s low observing frequency and wide bandwidth between 400–800 MHz contribute to the precision of our measurements, whereas the high cadence observation provide extremely high signal-to-noise co-added data. Our results represent a significant increase of the pulsar RM census, particularly regarding the northern hemisphere. These new RMs are for sources that are located in the Galactic plane out to 10 kpc, as well as off the plane to a scale height of ~ 16 kpc. This improved knowledge of the Faraday sky will contribute to future Galactic large-scale magnetic structure and ionosphere modelling.

Key words: pulsars: general – techniques: polarimetric – ISM: magnetic fields

1 INTRODUCTION

Radio pulsars have emission that is among the most polarized of all astronomical sources. As the linearly polarized emission travels through the interstellar medium (ISM) in the presence of magnetic fields, free electrons along the line of sight (LOS) lead to Faraday rotation of the observed pulsar radio emission. The differential of Faraday rotation (or the change in polarization angle, ΔPA) between two observing frequencies is associated to the Rotation Measure (RM) and the observing wavelength (λ):

$$\Delta\text{PA} = \text{RM}\lambda^2. \quad (1)$$

RM is in turn related to the number density of the free electrons along the LOS and the magnetic field of the LOS plasma (B) by:

$$\text{RM} = 0.812 \text{ rad m}^{-2} \int_0^d \left[\frac{n_e(s)}{\text{cm}^{-3}} \right] \left[\frac{B(s)}{\mu\text{G}} \right] \cdot \left(\frac{ds}{\text{pc}} \right), \quad (2)$$

where d is the distance to the pulsar. At the same time, the pulsar emission is dispersed by the plasma electrons. The ratio of the RM to the dispersion measure (DM) provides

an estimate of the integrated magnetic field strength along the parallel LOS:

$$\langle B_{\parallel} \rangle = 1.232 \mu\text{G} \left(\frac{\text{RM}}{\text{rad m}^{-2}} \right) \left(\frac{\text{DM}}{\text{pc cm}^{-3}} \right)^{-1}. \quad (3)$$

The Faraday rotation of pulsars is thus a powerful tool for studying the Galactic magnetic field. The study of magnetic field structure is important as it plays a critical role in numerous astrophysical processes, see for example, a review by Noutsos (2012). Currently in the *ATNF Pulsar Catalogue*¹ (V1.61; Manchester et al. 2005), there are 1167 pulsars with a published RM, which is approximately 42% of the full pulsar population. These pulsars are distributed throughout the Galactic disc, mapping the $\langle B_{\parallel} \rangle$ of over a thousand LOS. Numerous previous studies have used pulsar RMs to model the large-scale component of the Galactic magnetic field (GMF; Noutsos et al. 2015; Han et al. 2018; Sobey et al. 2019). Pulsar RMs can also be combined with

¹ <http://www.atnf.csiro.au/research/pulsar/psrcat>

extragalactic RMs for a more comprehensive view of the Galactic disc and halo (e.g. [Van Eck et al. 2011](#)).

There is room for improvement in using pulsar RMs to model the GMF. Currently, a large fraction of the available pulsar RMs are located near the Galactic plane and are concentrated within a few kiloparsec from the Sun. Most of the previously measured RMs were obtained with the Australian Parkes telescope in the southern hemisphere which operates at 1.4 GHz. Since Faraday rotation depends on wavelength squared (Eq. 1), lower frequency observations lead to more precise measurements of RMs. Multiple aperture array telescopes at low frequency have come online in recent years. They will be providing an enhanced view of the polarized sky. These facilities include the Low-Frequency Array (LOFAR; [van Haarlem et al. 2013](#)), the Long-Wavelength Array (LWA; [Taylor et al. 2012](#)), the Murchison Widefield Array (MWA; [Tingay et al. 2013](#); [Wayth et al. 2018](#)). Most recently, the Canadian Hydrogen Intensity Mapping Experiment (CHIME; [CHIME/FRB Collaboration et al. 2018](#)), which is a dense-packed interferometer operating at 400–800 MHz, has also begun commissioning observations.

In this paper, we present a study of pulsar RMs using CHIME data. An overview of the telescope and observational data is provided in Section 2 and the method of analysis is detailed in Section 3. We report on our results in Section 4, including 55 new RMs as well as improvement in the uncertainties of 25 catalogue RM values. In Section 5, we discuss the implications of our work and conclude in Section 6.

2 TELESCOPE OVERVIEW AND OBSERVATIONS

2.1 The CHIME/Pulsar backend

CHIME is a radio telescope hosted by the Dominion Radio Astrophysical Observatory (DRAO) in British Columbia, Canada. CHIME operates across a wide bandwidth of 400–800 MHz and has a collecting area ($\sim 80 \times 100 \text{ m}^2$) and point-source sensitivity comparable to that of other 100-m class radio telescopes. The reflecting surface of CHIME consists of four parabolic cylinders. It is a transit telescope with no moving parts. For the CHIME/Pulsar project, we combine the signals from the 1024 dual polarization feeds and form 10 tied-array beams that are available as raw voltages ([Ng 2018](#)). This means we can track 10 different pulsars at any given time as they transit through CHIME’s field-of-view, along the meridian. This provides very high cadence scheduling: while many of the northern hemisphere pulsars are being monitored daily, the longest cadence to cycle through all sources in the northern sky is only ~ 10 days. This is reflected in the long co-added integration length of our data ($\text{Total}_{\text{fold}}$) and the high signal-to-noise (S/N) achieved as listed in Table A1. The transit time of each source is a function of the declination; transit times can range from tens of minutes to hours for circumpolar sources. CHIME can in principle observe down to a declination of -20° .

2.2 Observations and Data Types

The beamformed baseband data of the CHIME/Pulsar backend are dual-polarization, complex-sampled and split into 1024 frequency channels with 8 bits per complex sample. For each observing scan, we generate ‘fold mode’ archives using the ‘Digital Signal Processing for Pulsars’ (`dspsr`) suite, an open source GPU-based library developed by [van Straten & Bailes \(2011\)](#). These data are coherently dedispersed at the known DM (taken from the ATNF catalogue) and then folded at the catalogue spin period with nominally 256 phase bins at 10 s sub-integration and the four Stokes (I , Q , U , and V) parameters are recorded. While 256 phase bins should be adequate for most of the pulsars studied in this work, we note that using too few phase bins could potentially lead to depolarization. A number of our pulsar observations were recorded with up to 2048 phase bins. For these sources, we step through the range of 32 to 2048 phase bins and see no obvious trend in the resulting RMs that is greater than their uncertainties.

The data have not yet been polarization calibrated. The beam shape of any aperture array is complicated, especially in the case of CHIME where over a thousand analog input components are involved. A proper calibration will be implemented in the near future. Fortunately, Faraday rotation is generally unaffected because there are no wavelength-squared dependencies in the beam shape. We have verified our RM analysis pipeline by cross checking with 100 pulsars with catalogue RMs and obtained consistent results for most of them (see Section 4.1). We note that uncalibrated data could potentially show instrumental polarization, where emission from Stokes I contaminates the other Stokes parameters. This is manifested as a peak in the Faraday spectrum centred at zero; see for example, PSRs J0026+6320, J0324+5239, B0331+45, J0426+4933 in Fig C1. For a discrete sampled Faraday dispersion function, the FWHM of the theoretical RM spread function (RMSF) is given by $\delta\phi = 3.8/\Delta(\lambda^2)$ ([Brentjens & de Bruyn 2005](#)). For CHIME, we have a $\delta\phi$ of about 9 rad m^{-2} . The majority of our RM values have a higher magnitude than this so the presence of leakage does not cause any confusion. However, this could have an effect on small RMs and is further discussed in Section 4.2.

3 DATA REDUCTION AND ANALYSIS

Our offline data analysis pipeline is heavily based on modules from the `psrchive` pulsar data processing ([Hotan et al. 2004](#); [van Straten et al. 2012](#)). First, data affected by radio frequency interference (RFI) are excised by identifying outlier intensity values both in time and frequency. These sub-integrations and frequency channels are set to zero using `paz` and `pazi`. We create updated pulsar ephemerides using the `tempo2` software package ([Hobbs et al. 2006](#)) and we fit for DM using `pdmp` in order to properly co-add all available fold mode data to obtain the highest possible S/N. The S/N-optimized DM for each pulsar is listed as DM_{obs} in Table A1. We have not taken into account any temporal DM variations in this work. DM variations up to the order of $10^{-2} \text{ cm}^{-3} \text{ pc/yr}$ have been reported in the literature (see, e.g. [Lam et al. 2015](#)). We have verified that offsetting the

folding DM by this amount does not lead to difference in RM greater than the RM uncertainty quoted here.

We quantify the RM of these co-added data using the `rmfit`² tool. An initial guess of the RM is found by brute force searching the RM range of $\pm 1500 \text{ rad m}^{-2}$. At each trial RM, `rmfit` corrects for the associated Faraday rotation and computes the total linear polarization $L = (Q^2 + U^2)^{1/2}$ across the on-pulse region. `rmfit` then fits a Gaussian to the resultant RM spectrum to identify a peak RM. This RM value is then iteratively refined as follows: the data are split in two equal frequency bands where each data segment is integrated and then compared to compute a weighted differential Δ PA. The uncertainty of Δ PA is minimized to obtain the best-fit RM value. Previous studies such as Morello et al. (2020) have shown that the iterative method of `rmfit` can sometimes under-estimate the RM uncertainty. For pulsars that have high enough S/N for RM to be obtained on a per-session basis (i.e., without having to co-add across multiple days), we use the spread of one standard deviation of these daily RM values as our uncertainty. This applies to 39 out of the 80 updated RMs reported in this work. For the remaining pulsars which are too weak to obtain per-session RM, we adopt the RM uncertainty given by the brute-force method of `rmfit` on the co-added data, which is conservatively calculated to be the range where the Gaussian fit for the RM spectrum drops by $2\text{-}\sigma$.

Unmodelled profile evolution could lead to the addition of sine waves with amplitudes that have different frequency dependence and potentially introducing bias in the RM measurement. Profile evolution is expected to be most rapid at lower observing frequencies below 200 MHz (see, e.g. Phillips & Wolszczan 1992). Upon a visual inspection, we do not see substantial variations among the pulsars in this sample and so have not attempted to fit for 2-D pulse profiles. The effect of ionospheric Faraday rotation has not been corrected in this work. To do that properly requires a careful modelling of the ionosphere and is out of scope for this project. However, all the observations on which this paper is based were obtained during the current minimum of solar activity. We estimate that ionospheric RM was usually less than 1 rad m^{-2} , and no more than $+2 \text{ rad m}^{-2}$ even during daytime (Mevius 2018b,a).

4 RESULTS

4.1 Comparison to catalogue RMs

The data set used in this work is from the first year of CHIME/Pulsar commissioning observations, which spans September 2018 to 2019. In order to verify our RM pipeline and the CHIME data, we first attempt to cross check RMs for pulsars that have a catalogue RM value. We analyse all pulsars above declination $\delta = 0^\circ$ detected by CHIME that have a published RM between $\pm 100 \text{ rad m}^{-2}$. We detect unambiguous RMs in 100 pulsars and use them as our verification sample. As can be seen from Fig. 1, most of our observed RM (RM_{obs}) agree with the catalogue value (RM_{cat}), which is reassuring. In addition, we measure RMs with substantially lower uncertainties than those in the ATNF pulsar

catalogue (V1.61) for 25 pulsars. This is likely due to the higher precision RM made possible from our lower frequency and large bandwidth observations, as well as the high S/N profiles, which result from long-duration co-added data.

Eight of the RMs we measure differ significantly from their catalogue values. These sources are annotated in Fig. 1. The catalogue RM of three of those, namely PSRs J0538+2817, J0546+2441, and J0751+1807, are close to zero, which suggests that previous studies might have been contaminated by spectral leakage. We find that the RMs of four pulsars have changed by a few to a few tens of RM units in the time between their catalogue measurement epochs and our more recent CHIME detections. These include PSR B0144+59 with $\text{RM}_{\text{cat}} = -19(4) \text{ rad m}^{-2}$ (Rand & Lyne 1994) compared to $\text{RM}_{\text{obs}} = -9.5(5) \text{ rad m}^{-2}$, PSR B1612+07 with $\text{RM}_{\text{cat}} = 40(4) \text{ rad m}^{-2}$ (Hamilton & Lyne 1987) compared to $\text{RM}_{\text{obs}} = 28(3) \text{ rad m}^{-2}$, PSR B2148+52 with $\text{RM}_{\text{cat}} = -44(11) \text{ rad m}^{-2}$ (Mittra et al. 2003) compared to $\text{RM}_{\text{obs}} = -19.0(8) \text{ rad m}^{-2}$, and PSR J2240+5832 with $\text{RM}_{\text{cat}} = 24(4) \text{ rad m}^{-2}$ (Theureau et al. 2011) compared to $\text{RM}_{\text{obs}} = 17.1(11) \text{ rad m}^{-2}$. These differences are too big to be explained by any ionospheric corrections. It is possible that we are seeing a genuine temporal evolution of these RMs over the years, although there are no other data points in the literature to help verify this. The presence of an unusual local environment (e.g. the Supernova Remnant of Vela (Johnston et al. 2005), an eclipsing black widow binary (Breton et al. 2013)) has been suggested to cause a change in temporal RM, although these scenarios do not seem to apply to the four pulsars listed above. Finally, for PSR B0331+45 we obtain an RM_{obs} of $-15.2(11) \text{ rad m}^{-2}$ which is discrepant with the latest result from Sobey et al. (2019) at $5.60(9) \text{ rad m}^{-2}$. Even though our data of PSR B0331+45 is affected by instrumental leakage which shows up as a peak near zero in the RM spectrum (see Fig. C1), we detect a clear non-zero RM and the signal is confirmed upon inspecting the expected oscillation in Stokes Q . Given that our work and that of Sobey et al. (2019) are taken relatively close in time, it seems unlikely that the RM could have changed so much within a year or so. We note that there is an older published RM of this pulsar at $-41(20) \text{ rad m}^{-2}$ by Rand & Lyne (1994), which is consistent with our observed value.

4.2 New RMs for 55 pulsars

Over 500 known pulsars were detected by CHIME/Pulsar above $\delta = -20^\circ$ in the first year of commissioning. We have sufficiently high S/N data for RM measurement for 109 of these pulsars that do not already have published RM values. We obtain new RMs for 55 of these pulsars; see Table A1 for details, and Figs. C1-C3 for the individual RM spectra. We are not able to quantify RMs for the remaining pulsars because of two reasons: (1) instrumental leakage dominates 30 of those, which could potentially be improved when a polarization calibration scheme is carried out on CHIME data in the future; (2) no RM peak is detected in 24 pulsars, which could be because these pulsars are intrinsically weakly polarized. Refer to Appendix C for a list of these pulsars.

Thirteen of these 55 pulsars were already studied using LOFAR in Sobey et al. (2019), although they did not detect any significant RM at the time (refer to Table 2 in that pub-

² <http://psrchive.sourceforge.net/manuals/rmfit/>

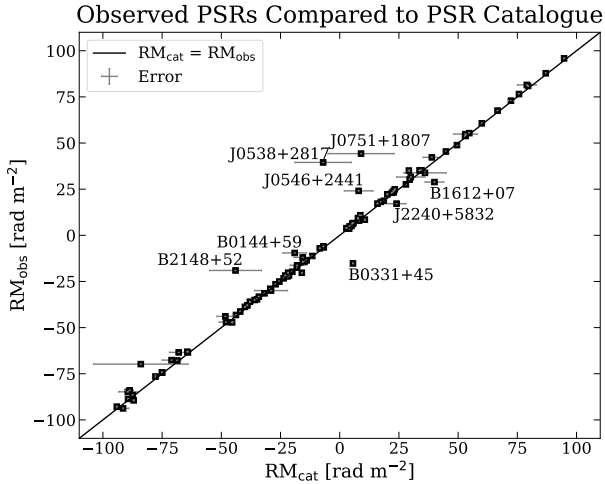


Figure 1. A comparison between RM_{obs} and RM_{cat} for 100 pulsars above $\delta = 0^\circ$ detected by CHIME. The black line corresponds to the $RM_{\text{obs}} = RM_{\text{cat}}$ trend which we expect to see. PSRs B0144+59, B0331+45, J0538+2817, J0546+2441, J0751+1807, B1612+07, B2148+52 and J2240+5832 are highlighted as they significantly deviate from the $RM_{\text{obs}} = RM_{\text{cat}}$ trend; these eight pulsars are discussed further in the main text.

lication). This may be because LOFAR’s frequency channel widths are sufficiently broad that they lose $>50\%$ sensitivity for $|RM| > 163 \text{ rad m}^{-2}$, whereas for CHIME/Pulsar, with our frequency resolution of 390 kHz, we maintain full sensitivity out to a RM of roughly 1000 rad m^{-2} . Some of these pulsars lie along the Galactic plane, and LOFAR could be suffering from more scattering and depolarization at the high DM and RM due to its low observing frequency. We note that there is likely some degree of profile scattering for some of the pulsars in the CHIME band as well. We have not attempted to model the effect of scattering on RM here; the difference is expected to be small and within the uncertainty of our RM values. Finally, the remarkably long duration from the co-addition of data significantly increases our ability to conduct this kind of analysis on a large number of pulsars that would otherwise not have the required S/N to robustly measure the RM.

As mentioned before, the data configuration of CHIME implies that we have a theoretical RMSF of $\sim 9 \text{ rad m}^{-2}$. Three of our new RMs fall within this range, notably PSR J1647+6608 with $RM_{\text{obs}} = 7(3) \text{ rad m}^{-2}$, PSR J1911+1347 with $RM_{\text{obs}} = -7(3) \text{ rad m}^{-2}$, and PSR J2340+08 with $RM_{\text{obs}} = -7(2) \text{ rad m}^{-2}$. Judging from their respective RM spectrum (see Fig. C1–C3), the RM peak is clearly distinct from zero. This made us believe that these new RMs are reliable and not due to confusion with instrumental leakage.

5 DISCUSSION

We have updated 25 existing RM values of northern hemisphere pulsars and measured 55 new RMs. These 80 pulsars are located in our full range of Right Ascension (RA) and δ , spanning $1.5^\circ \leq RA \leq 355.8^\circ$ and $-6.7^\circ \leq \delta \leq 83.2^\circ$. In terms of Galactic coordinates, which provide useful insight for studies looking at the Milky Way’s magnetic field along

longitudinal LOS, the pulsars lie within Galactic longitude of $20.6^\circ \leq l \leq 219.4^\circ$ and Galactic latitude of $-50.4^\circ \leq b \leq 54.2^\circ$. The range of updated RMs reported in this work lies between $-295 \text{ rad m}^{-2} \leq RM_{\text{obs}} \leq 338 \text{ rad m}^{-2}$. The average $|RM_{\text{obs}}|$ in this study is roughly 70 rad m^{-2} . Combining the DM_{obs} listed in Table A1, we can apply Equation 3 to calculate the LOS parallel magnetic field strength, $\langle B_{\parallel} \rangle$ (last column of Table A1). According to Sun & Reich (2010), the strength of the regular halo magnetic field is about $2 \mu\text{G}$, with which our results are largely consistent.

If we take into account the DM-derived distance of these pulsars as listed in the ATNF Pulsar Catalogue (based on the electron density model of Yao et al. 2017), we can locate the derived $\langle B_{\parallel} \rangle$ on a 3-D plot in Cartesian coordinates, as shown in Figs. C4–C6. Note that most of the known pulsars do not have independent distance measurements (e.g. from parallax), and a majority of the pulsar distances are obtained from their DM, combined with a model of the free electron distribution, which is said to have uncertainty up to some 20%. Keeping the caveat of the distance uncertainty in mind, we can still form an overview picture of the updated Faraday sky. In Fig. C4, we overlay the location of RM values from this work as well as all existing catalogue pulsar RMs with a simulation of the spiral arm structure of our Milky Way. It can be seen that most of our RMs fall within quadrants III and IV, and they also somewhat follow the arm structure. Compared to the recent LOFAR study by Sobey et al. (2019), we typically measure RMs farther out along the Galactic plane (up to $\sim 10 \text{ kpc}$) whereas LOFAR’s sample is mostly concentrated near the Sun. This is likely due to less severe scattering and depolarization at the higher observing frequency of CHIME. In terms of scale height (z), we cover a large range, detecting RMs up to $z \sim 16 \text{ kpc}$. From our 80 updated RMs, we see a similar dichotomy already mentioned by Sobey et al. (2019), that $\langle B_{\parallel} \rangle$ values above the Galactic plane tend to be positive while those below the plane tend to be negative.

6 CONCLUSIONS

We present new measurements of RMs for northern radio pulsars, using commissioning data from CHIME/Pulsar. We report 55 new RMs, and provide improved values and uncertainties for 25 pulsars with previously catalogued RMs. The wide bandwidth of CHIME has enabled our high RM precision. The observing frequency of 400–800 MHz is at a sweet spot for RM studies, low enough to take advantage of the wavelength squared dependency of RM and the steep spectrum of most pulsars, but not so low as to be hindered by scattering and depolarization at high DM and RM. The high cadence observations of CHIME also provide excellent S/N in our co-added data. We note that ionospheric RM corrections have not been applied in this work and it remains the biggest source of systematic uncertainty in our RMs.

The 80 updated RMs reported here cover a large region of the Milky Way, both deep in the Galactic plane and far out in the halo. The derived $\langle B_{\parallel} \rangle$ values are comparable to the average magnetic field strength of our Galaxy. Overall, this work improves our knowledge of the Faraday sky, with potential implications on future Galactic large-scale structure and ionospheric modelling studies.

ACKNOWLEDGEMENTS

We are grateful to the staff of the Dominion Radio Astrophysical Observatory, which is operated by the National Research Council Canada. Pulsar research at UBC is supported by an NSERC Discovery Grant and by the Canadian Institute for Advanced Research. CN is a SOSCIP TalentEdge fellow. AP was supported by the Summer Undergraduate Research Program (SURP) in astronomy & astrophysics at the University of Toronto. V.M.K. holds the Lorne Trotter Chair in Astrophysics & Cosmology and a Canada Research Chair and receives support from an NSERC Discovery Grant and Herzberg Award, from an R. Howard Webster Foundation Fellowship from the Canadian Institute for Advanced Research (CIFAR), and from the FRQNT Centre de Recherche en Astrophysique du Quebec. P.S. is a Dunlap Fellow and an NSERC Postdoctoral Fellow. The Dunlap Institute is funded through an endowment established by the David Dunlap family and the University of Toronto. We thank Tom Landecker for useful discussion and Bradley Meyers for carefully reading the manuscript. We also thank Jumei Yao for providing the electron density data for the YMW2016 model.

REFERENCES

- Brentjens M. A., de Bruyn A. G., 2005, *A&A*, **441**, 1217
 Breton R. P., et al., 2013, *ApJ*, **769**, 108
 Brinkman C., Freire P. C. C., Rankin J., Stovall K., 2018, *MNRAS*, **474**, 2012
 CHIME/FRB Collaboration et al., 2018, *ApJ*, **863**, 48
 Gentile P. A., et al., 2018, *ApJ*, **862**, 47
 Hamilton P. A., Lyne A. G., 1987, *MNRAS*, **224**, 1073
 Han J. L., Manchester R. N., van Straten W., Demorest P., 2018, *ApJS*, **234**, 11
 Hankins T. H., Rankin J. M., 2010, *AJ*, **139**, 168
 Hobbs G. B., Edwards R. T., Manchester R. N., 2006, *MNRAS*, **369**, 655
 Hotan A. W., van Straten W., Manchester R. N., 2004, *Publ. Astron. Soc. Australia*, **21**, 302
 Johnston S., Hobbs G., Vigeland S., Kramer M., Weisberg J. M., Lyne A. G., 2005, *MNRAS*, **364**, 1397
 Lam M. T., Cordes J. M., Chatterjee S., Dolch T., 2015, *ApJ*, **801**, 130
 Lynch R. S., et al., 2013, *ApJ*, **763**, 81
 Manchester R. N., Hobbs G. B., Teoh A., Hobbs M., 2005, *VizieR Online Data Catalog*, **7245**, 0
 Mevius M., 2018a, RMextract: Ionospheric Faraday Rotation calculator (ascl:1806.024)
 Mevius M., 2018b, in *Astrophysics and Space Science Library*. p. 103, doi:10.1007/978-3-319-23434-2_7
 Mitra D., Wielebinski R., Kramer M., Jessner A., 2003, *A&A*, **398**, 993
 Morello V., et al., 2020, *MNRAS*, **493**, 1165
 Ng C., 2018, in Weltevrede P., Perera B. B. P., Preston L. L., Sanidas S., eds, *IAU Symposium Vol. 337, Pulsar Astrophysics the Next Fifty Years*. pp 179–182 (arXiv:1711.02104), doi:10.1017/S1743921317010638
 Noutsos A., 2012, *Space Sci. Rev.*, **166**, 307
 Noutsos A., et al., 2015, *A&A*, **576**, A62
 Phillips J. A., Wolszczan A., 1992, *ApJ*, **385**, 273
 Rand R. J., Lyne A. G., 1994, *MNRAS*, **268**, 497
 Sobey C., et al., 2019, *MNRAS*, **484**, 3646
 Sun X.-H., Reich W., 2010, *Research in Astronomy and Astrophysics*, **10**, 1287
 Taylor G. B., et al., 2012, *Journal of Astronomical Instrumentation*, **1**, 1250004
 Theureau G., et al., 2011, *A&A*, **525**, A94
 Tingay S. J., et al., 2013, *Publ. Astron. Soc. Australia*, **30**, e007
 Van Eck C. L., et al., 2011, *ApJ*, **728**, 97
 Wayth R. B., et al., 2018, *Publ. Astron. Soc. Australia*, **35**, 33
 Yao J. M., Manchester R. N., Wang N., 2017, *ApJ*, **835**, 29
 van Haarlem M. P., et al., 2013, *A&A*, **556**, A2
 van Straten W., Bailes M., 2011, *Publications of the Astronomical Society of Australia*, **28**, 1
 van Straten W., Demorest P., Osłowski S., 2012, *Astronomical Research and Technology*, **9**, 237

APPENDIX A: SUMMARY OF RESULTS

Summarized in Table A1 are the principal results of this study using the `rmfit` tool on co-added pulsar observations from CHIME/Pulsar. This Table comprises 80 pulsars: 55 new RM results that have not been previously published and 25 updated RMs to the pulsar catalogue (version 1.61) with tighter bounds on the uncertainty.

Column 1 shows the pulsar name in B1950 or J2000 coordinate systems; the pulsars are listed in order of ascending RA. Columns 2–3 show the published RM results and uncertainties from the latest version of the ATNF pulsar catalogue (V 1.61) and column 4 includes a short-hand of the corresponding literature reference in which the result was published. The full citation of these entries can be found in Table A2. Asterisks in columns 2–4 denote results that do not have a previously published RM result in the pulsar catalogue. Column 5 lists the MJD range of our CHIME/Pulsar data set and column 6 indicates the total length of fold mode observation in the co-added data. The S/N of the co-added profile can be found in column 7. The DM and the RM obtained from the co-added data are tabulated in columns 8–11. The uncertainty of our observed RM comes from the spread of the per-session RMs. When that is not available for the low S/N pulsars, uncertainty is taken from the RM spectrum Gaussian fit width calculated by `rmfit`. Our RMs do not include any ionospheric corrections. Columns 12–13 list the $\langle B_{\parallel} \rangle$ and associated error derived from applying Equation 3 to our DM and RM results.

Table A1: Summary of 80 co-added RMs obtained in this work. See Appendix A for a detailed description of each column.

PSR	RM _{cut} (rad m ⁻²)	±	Ref	MJD	Total _{fold} (hrs)	S/N	DM _{obs} (pc cm ⁻³)	±	RM _{obs} (rad m ⁻²)	±	$\langle B_{\parallel} \rangle$ (μG)	±
J0006+1834	*	*	*	58441-58740	10.7	76	12.4606	0.2000	-20	3	-2.008	0.041
J0026+6320	*	*	*	58441-58467	1.2	82	245.1196	0.1000	-294	2	-1.483	0.002
J0058+6125	*	*	*	58441-58742	38.0	94	128.6608	0.2000	-212	2	-2.032	0.006
B0138+59	-48.00	3.00	hl87	58520-58711	38.4	1752	34.4630	0.4000	-47.0	1.1	-1.684	0.024
B0144+59	-19.00	5.00	rl94	58321-58720	34.2	811	40.0862	0.0700	-9.5	0.5	-0.294	0.004
B0154+61	-29.00	7.00	hl87	58520-58701	19.4	735	29.9132	9.0000	-29	3	-1.272	0.457
J0201+7005	*	*	*	58634-58732	42.0	144	20.8587	0.5000	-39	3	-2.320	0.071
J0324+5239	*	*	*	58441-58692	15.9	188	115.4211	0.1000	-126	3	-1.348	0.003
B0331+45	5.60	0.09	sbg+19	58398-58720	14.6	845	47.1117	0.1000	-15.2	1.1	-0.398	0.003
B0339+53	-84.00	20.00	mwkj03	58351-58715	17.6	606	68.0324	0.7000	-69.7	1.5	-1.264	0.016
J0340+4130	*	*	*	58520-58744	81.9	361	49.5823	0.0003	56.1	0.7	1.395	0.002
B0355+54	79.00	4.00	hl87	58318-58711	41.0	6561	57.1223	0.0600	81.5	0.3	1.758	0.003
J0426+4933	*	*	*	58500-58691	6.5	346	84.1850	0.3000	-169	7	-2.485	0.012
J0453+1559	*	*	*	58439-58688	7.6	103	30.2880	0.0100	-35	2	-1.435	0.018
J0517+2212	-16.00	0.00	bfrs18	58439-58714	10.9	1030	18.6769	0.0800	-20.2	1.6	-1.338	0.009
J0538+2817	-7.00	12.00	mwkj03	58321-58709	8.9	886	39.8826	0.0500	39	3	1.220	0.002
J0540+3207	*	*	*	58520-58701	19.2	370	61.9038	0.2000	13.7	1.8	0.273	0.004
J0546+2441	8.00	6.10	hmvd18	58320-58735	12.6	294	73.0922	1.0000	24	3	0.407	0.008
J0555+3948	*	*	*	58520-58744	19.6	183	36.7105	0.4000	9	3	0.325	0.015
J0613+3731	*	*	*	58518-58720	5.5	178	18.7556	0.2000	16	2	1.082	0.017
J0614+83	*	*	*	58702-58737	19.2	45	43.8689	0.4000	-13	3	-0.385	0.090
J0627+0649	*	*	*	58456-58692	2.9	113	86.5563	0.1000	179	3	2.555	0.004
J0646+0905	*	*	*	58519-58640	8.7	190	148.8859	0.3000	-149	2	-1.239	0.003
J0711+0931	*	*	*	58520-58744	8.5	127	46.0848	0.4000	62.8	1.1	1.684	0.018
J0740+6620	*	*	*	58517-58731	78.5	385	14.9626	0.0002	-36	2	-3.040	0.010
J0751+1807	9.00	14.00	hmvd18	58321-58701	11.2	149	30.2438	0.0010	44	3	1.803	0.006
J0815+0939	53.10	5.00	hmvd18	58321-58715	10.0	127	53.0660	0.2000	54	2	1.275	0.009
J0843+0719	*	*	*	58321-58715	9.4	48	33.5864	0.5000	40	4	1.506	0.037
J1434+7257	*	*	*	58516-58700	34.5	267	12.5997	0.0100	-9.7	1.2	-0.951	0.017
J1518+4904	-15.60	3.70	hmvd18	58441-58733	17.6	2714	11.6062	0.0100	-11.9	1.3	-1.271	0.013
J1538+2345	*	*	*	58520-58741	9.7	141	14.4737	1.0000	11.5	1.1	1.020	0.093
J1544+4937	*	*	*	58520-58742	54.5	248	23.2280	0.0008	9.8	1.9	0.523	0.010
B1612+07	40.00	4.00	hl87	58329-58715	11.9	440	21.2426	0.4000	28	3	1.677	0.042
B1639+36A	*	*	*	58359-58693	25.3	112	30.4310	0.0040	13	3	0.532	0.012
J1647+6608	*	*	*	58501-58742	22.5	107	22.7981	0.6000	7	3	0.411	0.017
J1710+4923	*	*	*	58542-58721	13.2	193	7.0826	0.0010	12	2	2.117	0.165
J1736+05	*	*	*	58450-58718	10.0	54	38.6724	0.3000	44	3	1.417	0.027
J1738+0333	36	9	gmd+18	58515-58744	35.3	70	33.7652	0.0040	33	3	1.235	0.027
B1802+03	38.90	3.70	hmvd18	58328-58711	39.2	285	80.8294	0.0800	42	2	0.644	0.005
J1821+0155	*	*	*	58683-58719	4.7	56	51.7499	0.0100	110	3	2.638	0.014

Continued on next page

Table A1 – continued from previous page

PSR	RM _{cat} (rad m ⁻²)	±	Ref	MJD	Total _{fold} (hrs)	S/N	DM _{obs} (pc cm ⁻³)	±	RM _{obs} (rad m ⁻²)	±	$\langle R_{\parallel} \rangle$ (μG)	±
J1834+10	*	*	*	58721-58739	2.0	23	78.0350	0.7000	97.0	1.7	1.533	0.041
J1900+30	*	*	*	58715-58739	3.9	128	71.7592	0.2000	121	2	2.094	0.011
J1911+1347	*	*	*	58472-58742	24.6	87	30.9806	0.0004	-7	3	-0.282	0.011
J1918-0642	*	*	*	58500-58742	31.7	102	26.5890	0.0030	-57	3	-2.648	0.207
B1926+18	*	*	*	58365-58660	3.0	49	111.5379	0.4000	174	2	1.931	0.012
J1946+2535	*	*	*	58443-58708	2.0	39	248.4199	0.1000	57	3	0.293	0.015
J1946+2611	-88.70	1.70	hmvdl18	58461-58662	3.3	93	165.3295	0.1000	-83.9	1.3	-0.626	0.002
B1952+29	-18.00	3.00	hl87	58501-58662	6.3	530	7.8782	0.1000	-16	2	-2.567	0.041
B2002+31	30.00	6.00	hl87	58520-58701	32.4	1451	234.5535	0.8000	31.5	0.8	0.166	0.001
J2010+2845	*	*	*	58450-58705	5.2	146	112.3273	0.2000	-233	3	-2.560	0.007
J2011+3331	*	*	*	58521-58664	13.4	172	298.3448	0.3000	235.6	0.5	0.973	0.002
J2013+3058	*	*	*	58441-58650	6.6	174	148.6652	0.1000	-145	3	-1.204	0.007
J2016+1948	*	*	*	58451-58661	7.2	131	33.7492	0.2000	-121	4	-4.419	0.033
J2017+5906	*	*	*	58509-58636	10.6	174	59.9378	0.1000	33	3	0.696	0.005
J2019+2425	-71	4	gmd+18	58521-58677	7.8	189	17.1985	0.0010	-67.6	0.6	-4.843	0.006
B2025+21	*	*	*	58448-58664	8.1	64	96.9408	0.1000	-210	2	-2.680	0.007
J2027+4557	*	*	*	58447-58717	8.5	368	229.4552	0.4000	337	3	1.815	0.004
J2040+1657	*	*	*	58445-58737	5.1	72	50.2550	0.3000	-98	2	-2.413	0.021
J2045+0912	-89.50	3.90	hmvdl18	58445-58737	21.7	338	31.3267	0.1000	-84.7	1.9	-3.337	0.015
J2047+5029	*	*	*	58487-58701	6.7	118	107.8448	0.1000	-121	4	-1.394	0.004
B2053+36	-68.00	4.00	hl87	58440-58700	43.2	3082	97.3875	0.0800	-63.4	0.3	-0.802	0.001
J2102+38	*	*	*	58440-58701	28.0	255	86.0513	0.4000	-74	2	-1.062	0.007
B2122+13	-48.30	3.60	hr10	58440-58711	9.9	242	30.1597	0.2000	-43	3	-1.797	0.016
J2138+4911	*	*	*	58440-58693	7.3	441	168.2636	0.2000	-143	3	-1.052	0.002
J2139+00	*	*	*	58445-58693	27.6	353	31.2913	0.1000	11	2	0.439	0.007
B2148+52	-44.00	11.00	mwkj03	58443-58715	57.5	1564	149.0138	0.1000	-19.0	0.8	-0.157	0.001
J2208+4056	*	*	*	58452-58722	13.2	76	11.7588	0.2000	-40	3	-4.316	0.106
J2208+5500	*	*	*	58439-58693	5.1	234	104.5698	0.3000	-87	3	-1.027	0.007
J2216+5759	*	*	*	58521-58722	12.7	184	167.3322	0.1000	-10.9	1.7	-0.081	0.001
J2217+5733	*	*	*	58456-58718	16.0	491	130.6711	0.4000	-90	3	-0.085	0.004
J2227+30	*	*	*	58456-58605	5.1	589	19.9559	0.3000	-58.3	1.9	-3.612	0.068
J2229+6114	*	*	*	58451-58664	16.1	484	204.9635	0.0200	-187	3	-1.129	0.001
J2234+2114	-91.50	2.50	hmvdl18	58652-58722	3.9	191	34.7371	0.5000	-93.7	1.8	-3.329	0.060
J2240+5832	24.00	4.00	tpc+11	58455-58701	17.8	357	263.4647	0.0500	17.1	1.1	0.080	0.001
J2243+1518	*	*	*	58440-58722	10.0	66	39.6448	0.2000	-35.5	0.5	-1.120	0.020
J2302+4442	*	*	*	58450-58709	45.0	269	13.7196	0.0005	19.1	1.6	1.715	0.004
J2310+6706	*	*	*	58440-58651	3.7	29	98.5726	0.7000	-16	2	-0.204	0.008
J2319+6411	*	*	*	58519-58731	9.8	1393	245.9455	0.0800	-48.8	1.2	-0.244	0.001
J2340+08	*	*	*	58519-58701	8.8	118	23.9234	0.1000	-7	2	-0.388	0.022
J2343+6221	*	*	*	58652-58701	65.7	303	155.8648	0.6000	-44.9	0.9	-0.356	0.002

Table A2. Summary of the references for the catalogue RMs listed in Table A1.

Shorthand	Reference	(lowest) Centre frequency (MHz)	Ionospheric RM corrected
bfrs18	Brinkman et al. (2018)	327	N
gmd+18	Gentile et al. (2018)	1400	N
hl87	Hamilton & Lyne (1987)	408	Y
hmvd18	Han et al. (2018)	774	Y
hr10	Hankins & Rankin (2010)	50	N
lbr+13	Lynch et al. (2013)	350/820	N
mwkj03	Mitra et al. (2003)	1400	N
rl94	Rand & Lyne (1994)	1400	N
sbg+19	Sobey et al. (2019)	110	Y
tpc+11	Theureau et al. (2011)	1100	N

APPENDIX B: SUMMARY OF FARADAY SPECTRA OBSERVATIONS

Figures C1 through C3 show the individual Faraday spectra of the 80 RM results presented in Table A1. The x-axes show the appropriate RM range that incorporates the peak RM values. The y-axes show normalized polarized flux in arbitrary units as our data are uncalibrated in polarization. Peaks centred at 0 rad m^{-2} and symmetric peaks about 0 rad m^{-2} are due to instrumental leakage discussed in Section 2. The RM_{obs} is shown as a vertical dashed line and its corresponding uncertainty is represented by vertical solid lines, although in almost all cases the uncertainty range is too small to visually separate the three lines. When available, the catalogue RM (RM_{cat}) is represented by a vertical red dash-dot line and its corresponding uncertainty region is marked by the shaded hatch.

APPENDIX C: PULSARS WITH NO DETECTED RM

In addition to the 80 RMs reported in this work, a further 54 pulsars were studied although no RM was detected in them. Instrumental leakage dominated 30 pulsars, namely PSRs J0023+0923, J0051+0423, J0243+6027, J0329+1654, J0458-0505, J0609+2130, J0611+1436, J0621+0336, J0630-0046, J0647+0913, J1125+7819, J1327-0755, J1501-0046, J1628+4406, B1740-13, J1744-1610, J1745-0129, J1802+0128, J1807+0756, B1810+02, J1820-0509, B1831-00, J2018+3431, J2048+2255, J2123+5434, J2206+6151, J2228+6447, J2325-0530, J2333+6145, and J2352+65. A further 24 pulsars likely have intrinsically weak polarization, namely PSRs J0103+54, J0139+5621, J0332+79, J0337+1715, J0645+80, J0652-0142, B1740-03, J1819-1318, J1842+0638, J1843+2024, J1846-0749, J1846-07492, J1848+0826, B1904+12, B1906+09, J1925+19, J1931+30, B1933+17, J1954+4357, B1957+20, J2002+30, J2013-0649, J2015+2524, and J2030+55.

This paper has been typeset from a $\text{T}_{\text{E}}\text{X}/\text{L}^{\text{A}}\text{T}_{\text{E}}\text{X}$ file prepared by the author.

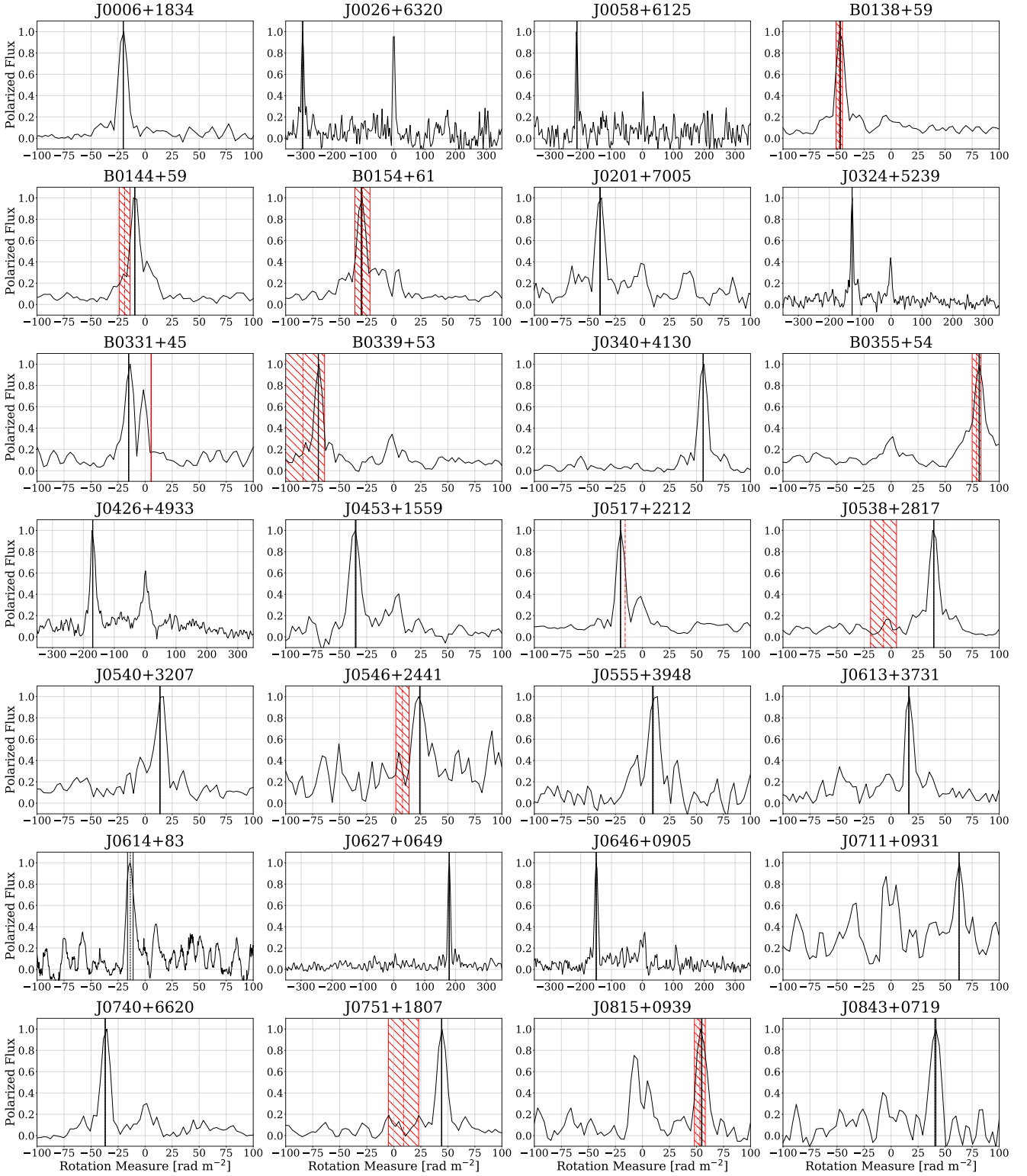


Figure C1. Faraday spectra of the 80 pulsars in this work. Refer to text for further description of the figures.

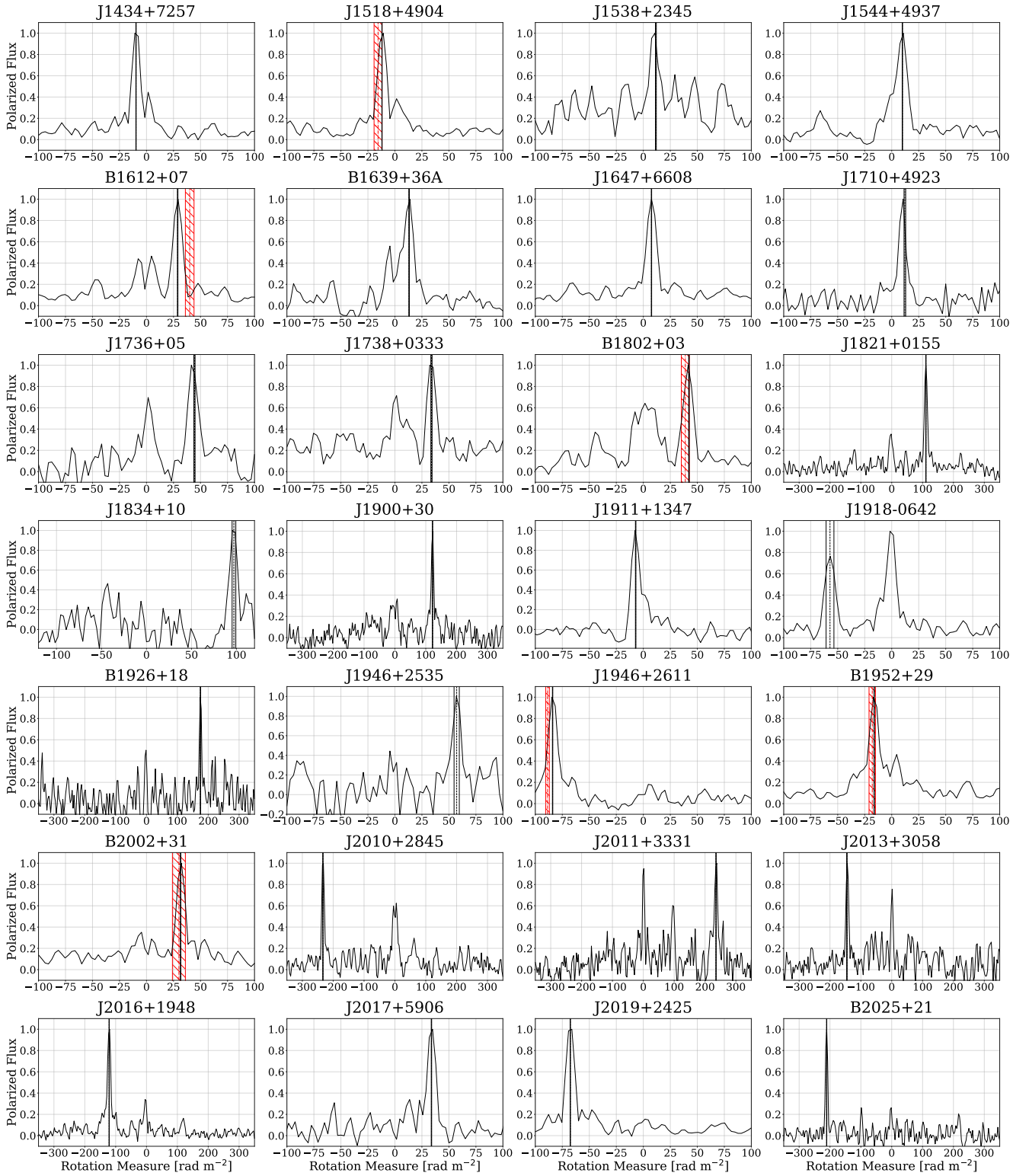


Figure C2. Continued from the previous page.

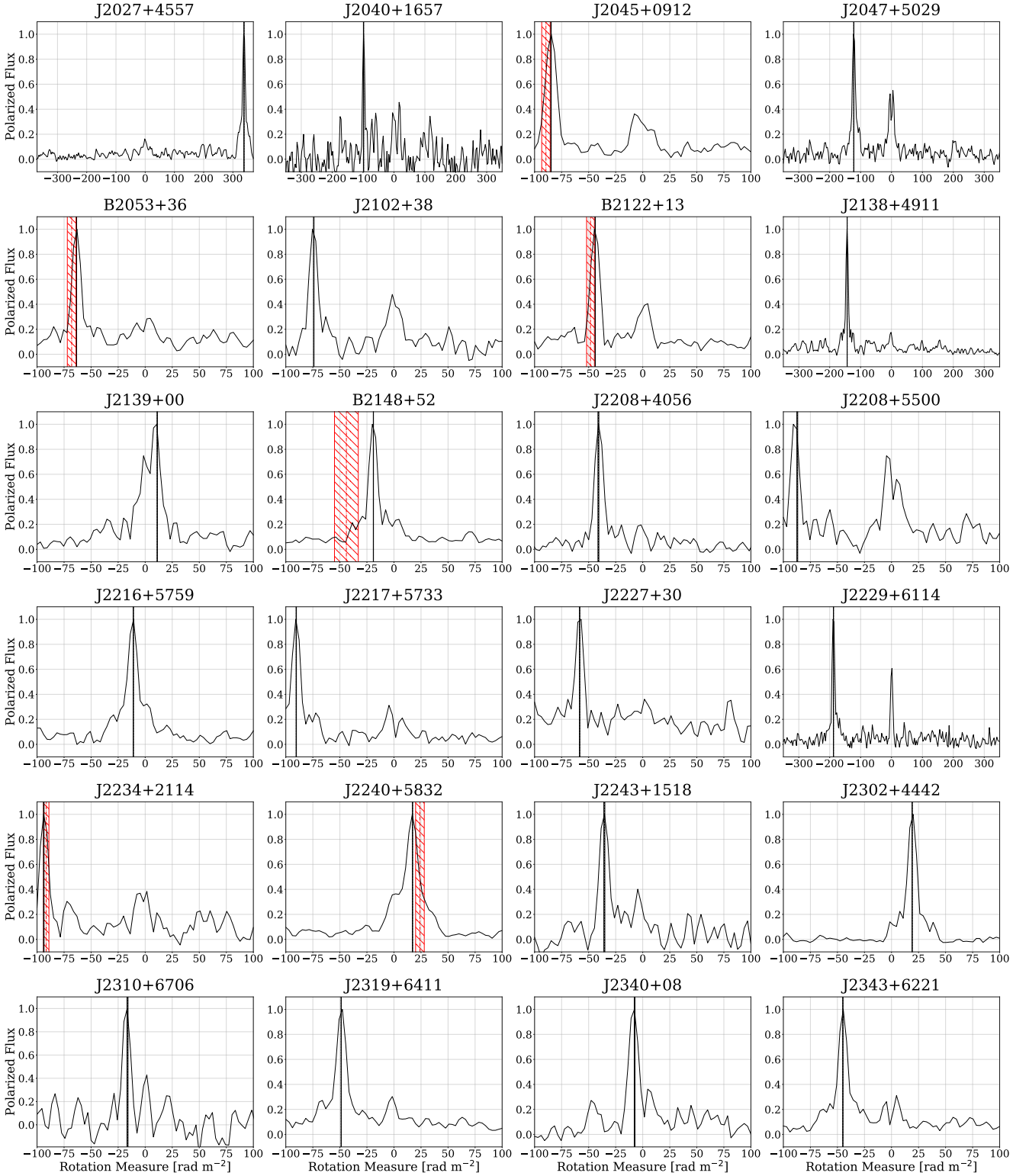


Figure C3. Continued from the previous page.

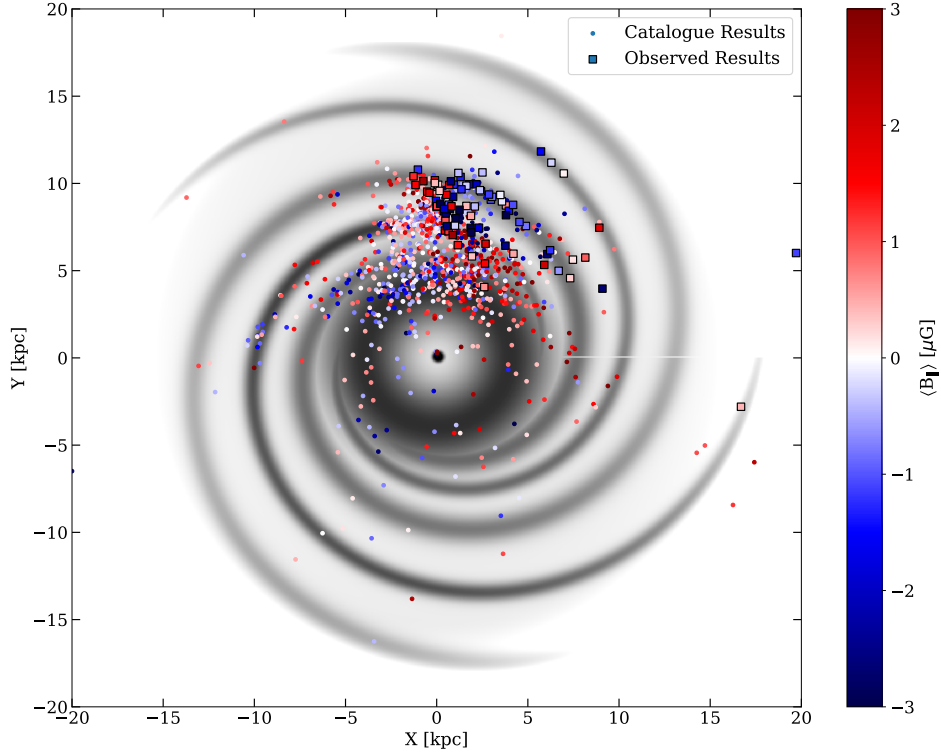


Figure C4. X-Y plane of the Milky Way, where the Sun is defined to be at $(X, Y) = (0, 8.3)$ kpc and the Galactic Centre at $(X, Y) = (0, 0)$ kpc. The pulsars with catalogue RM values are shown as circles, whereas the 80 updated RMs from this work are represented by squares. The colour scale of these symbols gives the $\langle B_{\parallel} \rangle$. Pulsars with $z > |16|$ kpc are not shown for clarity of the local distribution. The electron density in the plane of the Galaxy used in the YMW16 model is also shown in gray scale.

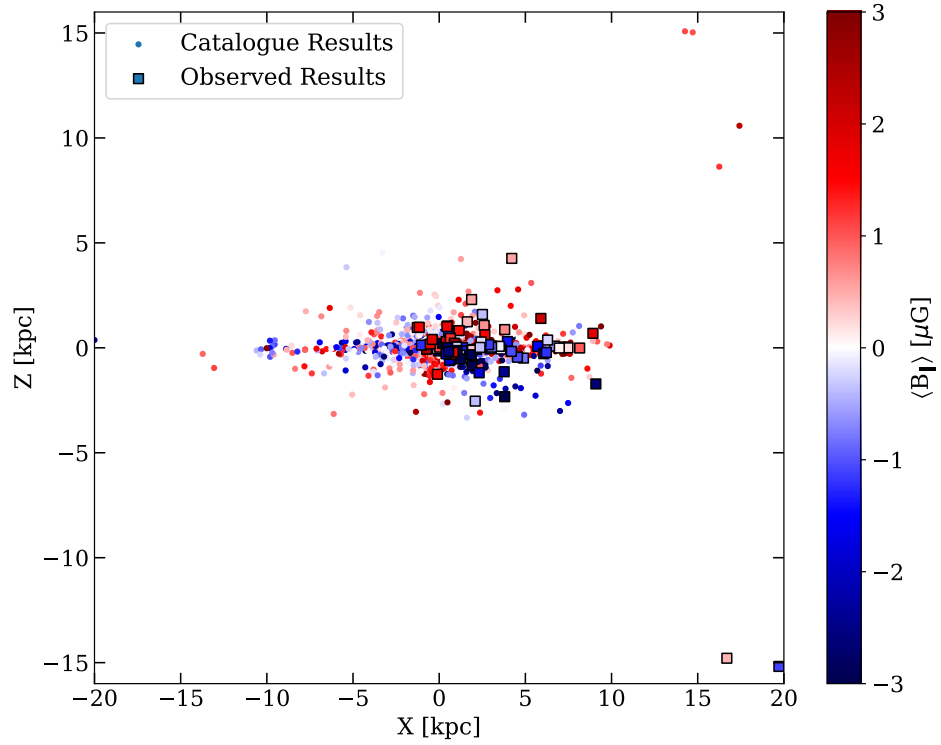


Figure C5. X-Z plane of the Milky Way, with the same plotting organization as Fig. C4.

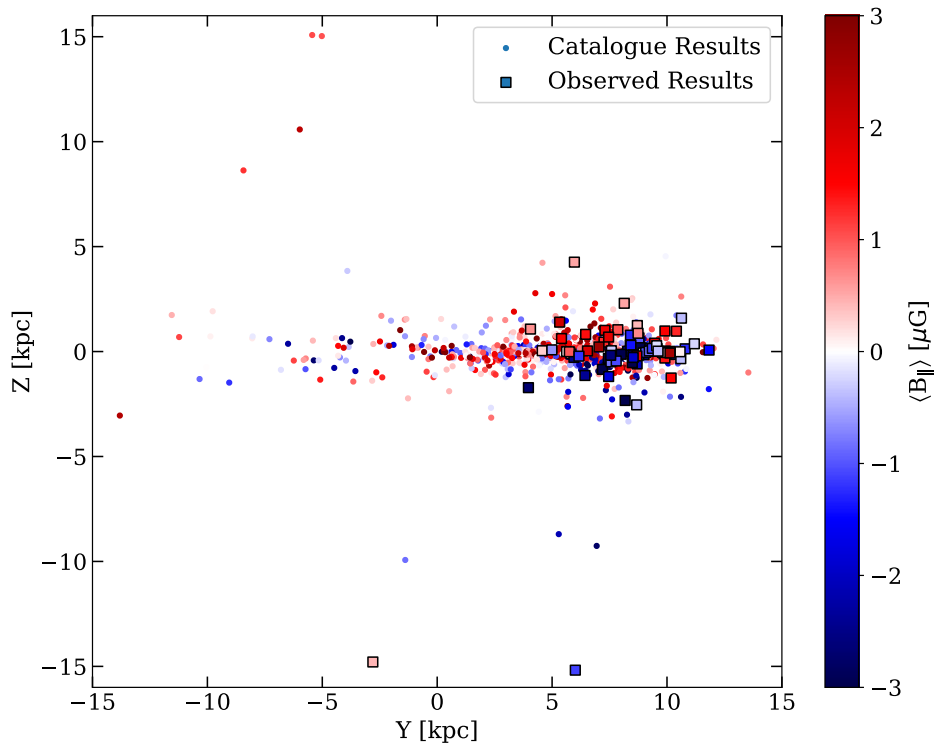


Figure C6. Y-Z plane of the Milky Way, with the same plotting organization as Fig. C4.